1
Quantum Dynamics of Molecular Elementary Processes in Catalytic Transformations

Günter Klatt and Horst Köppel

1.1
Introduction

Olefin insertion into an M–H bond and the reverse process, β-hydrogen elimination (BHE), represent elementary reaction steps that are of fundamental importance to many transition-metal (TM) catalyzed processes, such as hydrogenation, hydroformylation, and olefin polymerization, to mention a few. Correspondingly, there has been much theoretical effort toward characterizing the structural parameters and energetics of the intermediates and transition states [1–8], which complements the large amount of related experimental investigations (see, for example, Refs [9–12], and references therein).

Usually, the insertion proceeds in two steps, as is indicated in Scheme 1.1.

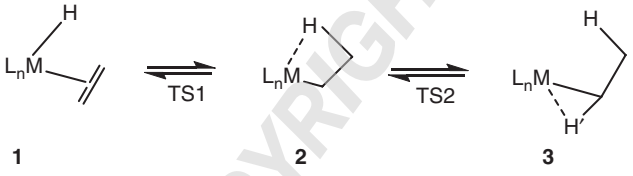

Scheme 1.1

Initially, the hydrogen atom migrates from the metal atom to which it is covalently bound in the olefin hydride structure **1** to the ethylene moiety to form the β-agostic structure **2**.

A further rearrangement yields the α-agostic complex **3**. These reaction steps are associated with the transition states TS1 and TS2 and are equilibrium processes, which are indicated by the harpoon arrows. For early TMs, such as titanium, zirconium, or chromium, the equilibrium favors the insertion products **2** and **3**. Catalytic ethylene homo- and copolymerization has been largely dominated by early TM catalysts [13–25], while late-metal catalysts generally show reduced activity and a strong tendency to form oligomers because the termination reactions involving the transfer of β-hydrogen atoms compete with chain

Molecular Catalysts: Structure and Functional Design, First Edition. Edited by Lutz H. Gade and Peter Hofmann.

growth [26]. In recent years, these disadvantages have been overcome by a new generation of late TM polymerization catalysts, based on the 1995 discovery of diimine complexes of Ni and Pd as active catalysts in ethylene polymerization by Brookhart and coworkers [27]. Compared to metallocene catalysts, these late TM catalysts are characterized by facile BHE, resulting in highly branched polymers with new physical properties. They also exhibit less oxophilicity and therefore a greater tolerance toward polar reagents. Much attention has since been paid to olefin polymerization using late TM catalysts (see, for example, Ref. [12], and references therein).

This chapter is organized as follows. First, the structural and energetic aspects of the migratory insertion/BHE in complexes of early (Cr) and late (Co, Rh) TMs will be discussed. These results are based on the application of density functional theory (DFT) to complexes of early and late TMs, in particular the isomers of Scheme 1.1. During the last decade, DFT has established itself as a useful and reliable method to study the potential energy surfaces (PESs) and reaction mechanisms of compounds containing TMs and heavy elements [28]. The subsequent section is dedicated to the application of quantum dynamical methods to TM-catalyzed olefin polymerization. The results presented here have been obtained using the wave packet methodology, which is based on the solution of the time-dependent Schrödinger equation and is well established and widely used for different kinds of systems (see, for example, Refs [29–33]). Unlike previously performed calculations at the Car–Parrinello molecular dynamics (CPMD) level [34, 35], this approach uses a full quantum treatment to describe the nuclear dynamics, which is of importance for describing coherence and tunneling effects, as well as the vibrational structure of electronic spectra. It describes the reaction path following a vertical Franck–Condon transition and allows the deduction of oscillation periods and lifetimes for the systems under study. Experimentally, the real-time monitoring of bond formation and bond cleavage can be studied by femtosecond time-resolved pump–probe spectroscopy [36–38], which relies on a quantum description of the nuclear motion. It also brings the system into a highly nonequilibrium initial state by the very nature of the excitation process.

1.2
Structural and Energetic Aspects

While the migratory insertion/BHE of the $[CpM(L)(H)(C_2H_4)]^+$ complexes is characterized by the five stationary points depicted in Scheme 1.1, additional isomers may be relevant for the insertion into a metal–alkyl bond. For example, for M = Cr it is known that the initial insertion product of the ethylene–alkyl complex I is a γ-agostic complex IIγ, which subsequently isomerizes to β- and α-agostic species IIβ and IIα [26], as shown in Scheme 1.2.

For this system, the probable catalytic cycle and possible termination reactions for the polymerization of ethylene have been investigated for model donor ligands containing phosphorus or nitrogen ($L = PH_3$, PMe_3, NMe_3) [39]. The starting

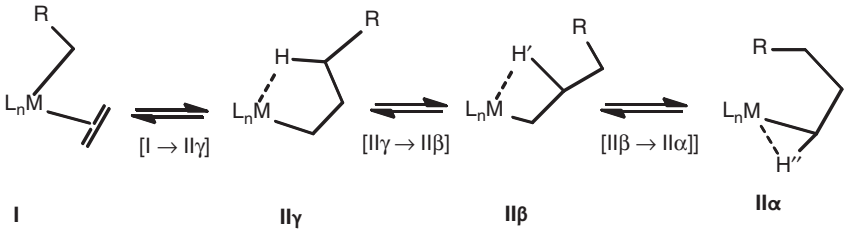

Scheme 1.2

point for these calculations was the cation $[CpCr(L)C_3H_7]^+$. The propagation and termination reactions are shown in Figure 1.1, starting with the insertion of ethylene into the Cr–C bond. Here, minima are designated by Roman numerals (I–VI), which in the case of an agostic structure Cr–H–C are followed by a Greek letter identifying the carbon atom involved. Transition states are labeled by the connected reactant and product states separated by an arrow and enclosed in square brackets. While the cationic Cr(III) complexes considered here usually have a quartet spin ground state, a possible termination process by β-hydrogen transfer (BHT) to a monomer involves a change of spin to the doublet state; in the following, the molecular term symbol is provided in parentheses where necessary (high-spin quartet configuration ^{4}A or low-spin doublet configuration ^{2}A).

The catalytic cycle shown at the top of Figure 1.1 consists of four intermediates, which differ by the kind of agostic interaction displayed (none, α-, β-, or γ-agostic). The insertion step always leads to the γ-agostic isomer as the initial product, except for the insertion of ethylene into the Cr–H bond, as there is no γ-H atom in the resulting complex [39]. Furthermore, two alternative mechanisms for the termination of the polymerization process exist:

- BHE involving the transfer of a hydrogen atom to the metal center and subsequent dissociation of the resulting olefin;
- BHT, in which the hydrogen is transferred to a monomer unit also coordinated to the metal, and which is thought to involve a change in spin multiplicity from the quartet to the doublet state.

The relative energies E and free energies G_{298} for the first two insertion steps with ligands L = (PH_3, PMe_3, NMe_3) are given in Figure 1.2. The findings confirm the rate-determining character of the insertion of ethylene into the chromium–alkyl bond, with an insertion barrier $\Delta E^{\ddagger} = 8.7 - 10.1$ kcal mol^{-1} for the first insertion step. Unlike Jensen *et al.* [26], we find that the coordination of ethylene proceeds from the β-agostic isomer IIβ, which represents the global minimum and resting state of the catalytic cycle. First, an "outer" van der Waals complex $II^{vdW}\beta$ is formed, in which the ethylene is loosely bound to IIβ, which then rearranges via a transition state $[II^{vdW}\beta \rightarrow I']$ to the ethylene complex I′.[1)]

1) The primed (′) complexes contain an additional ethylene unit in comparison to the preceding complexes.

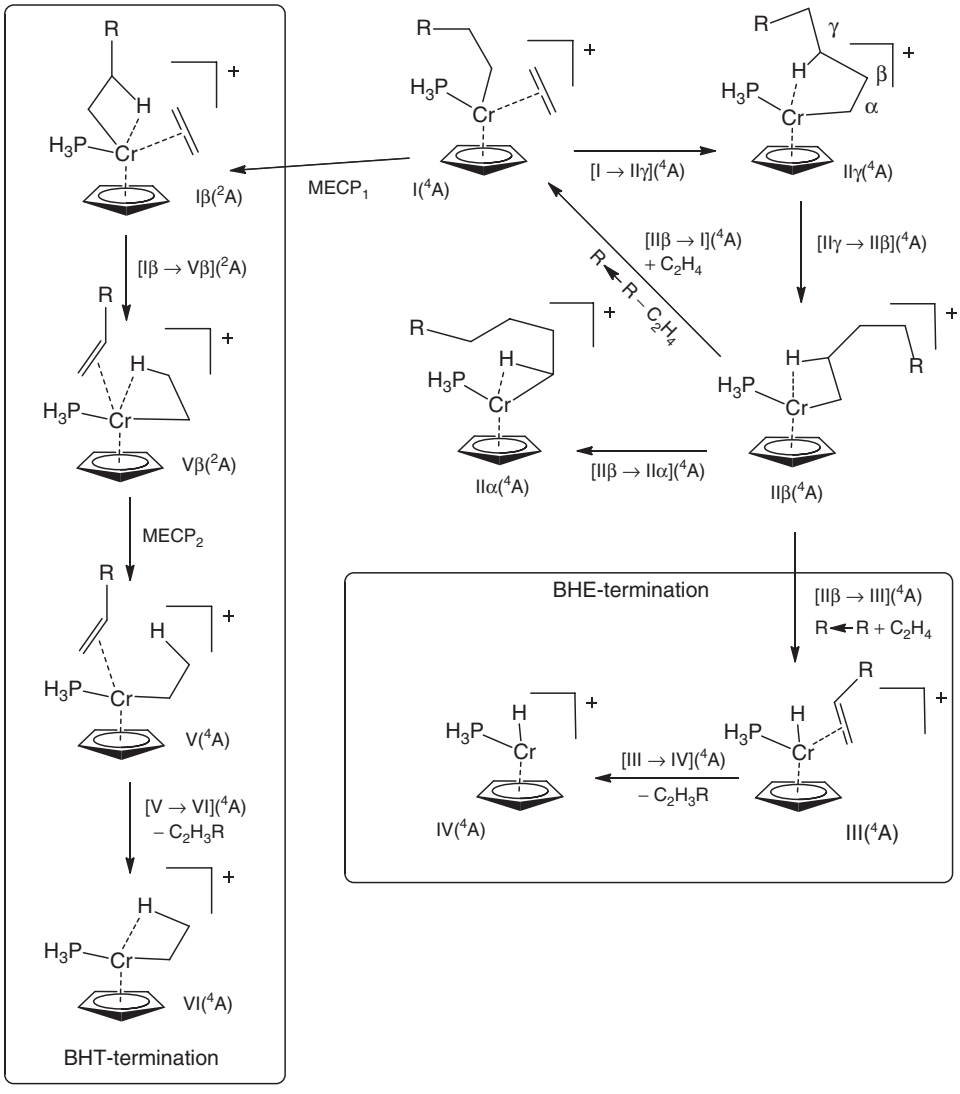

Figure 1.1 Catalytic cycle for the propagation reaction of $[Cp(PH_3)Cr\text{-}C_2H_4R]^+$ with ethylene (top), and the corresponding termination reactions by β-hydrogen elimination (BHE, bottom) or β-hydrogen transfer (BHT, left); method DFT (BP86/6-31G**/SDD(Cr)), R = H. Note that R becomes $R–C_2H_4$ for the process indicated by the diagonal arrow.

This result was confirmed by intrinsic reaction coordinate (IRC) calculations and is indicated by the diagonal arrow in Figure 1.1. The overall reaction is strongly exothermic ($\Delta E > 30$ kcal mol^{-1}), with only minor differences existing for the three ligands L. The insertion barriers [I → IIγ] are comparable in energy and lower by only about 1 kcal mol^{-1} for the more compact NMe_3 ligand in

the first insertion step; this effect becomes more pronounced for the second ethylene insertion because of the increased steric demand of the propyl residue. Comparing the values for E and G_{298}, it is noticed that the reaction is exergonic by only about 20 kcal mol^{-1} because of the decrease in particle number and hence entropy during propagation. The connectivities given in Figure 1.2 are not intended to suggest the existence of a single sequential reaction path but have been selected for illustrative purposes; the actual reaction path is branched because of the existence of interconnected pathways between all agostic isomers ($\alpha \leftrightarrow \beta$, $\alpha \leftrightarrow \gamma$, $\beta \leftrightarrow \gamma$).

The termination of the polymerization reaction by BHE to the chromium center and subsequent dissociation of the resulting olefin is found to require about 25 kcal mol^{-1} and to be thermodynamically much less feasible than the alternative termination process by BHT to a monomer. The latter process involves spin change; two minimum-energy crossing points (MECPs) and further transition states and intermediates have been identified [39]. The termination reaction may also be controlled by the use of polymerization additives [40].

A different picture is obtained for the migratory insertion into the M–H bond in late TMs according to Scheme 1.1. From inspection of the stationary points of the insertion in the $[CpRh(PH_3)(H)(C_2H_4)]^+$ complex in Figure 1.3, it follows that

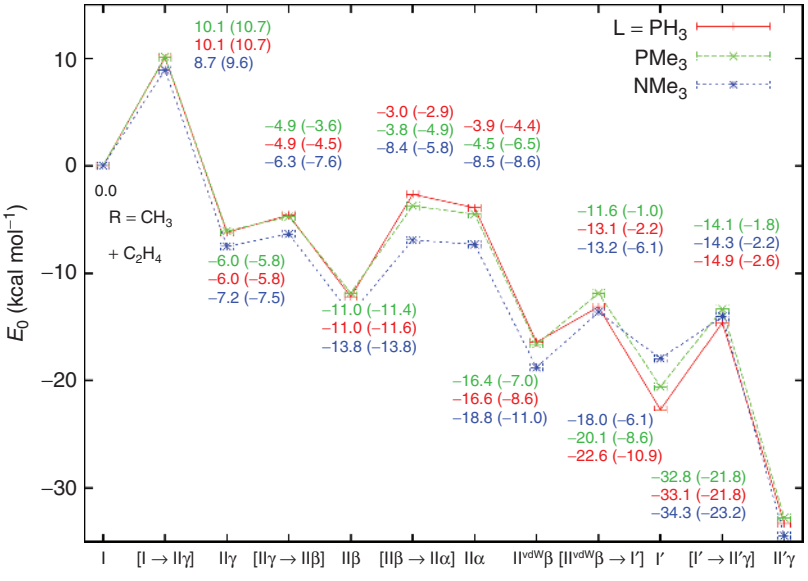

Figure 1.2 Energy profile for the first two insertion steps of the catalytic cycle for the complex $[Cp(L)Cr(C_2H_4)R]^+$ for R = CH_3 and L = PH_3, PMe_3, or NMe_3. All energies are corrected for zero-point vibrational energy and include the energy of separate C_2H_4 where required. Free energy values G_{298} are added in parentheses. For labels see Figure 1.1. The primed (′) complexes contain an additional ethylene unit in comparison to the preceding complexes, while for complex $II^{vdW}\beta$ the ethylene is attached to IIβ by van der Waals interactions only.

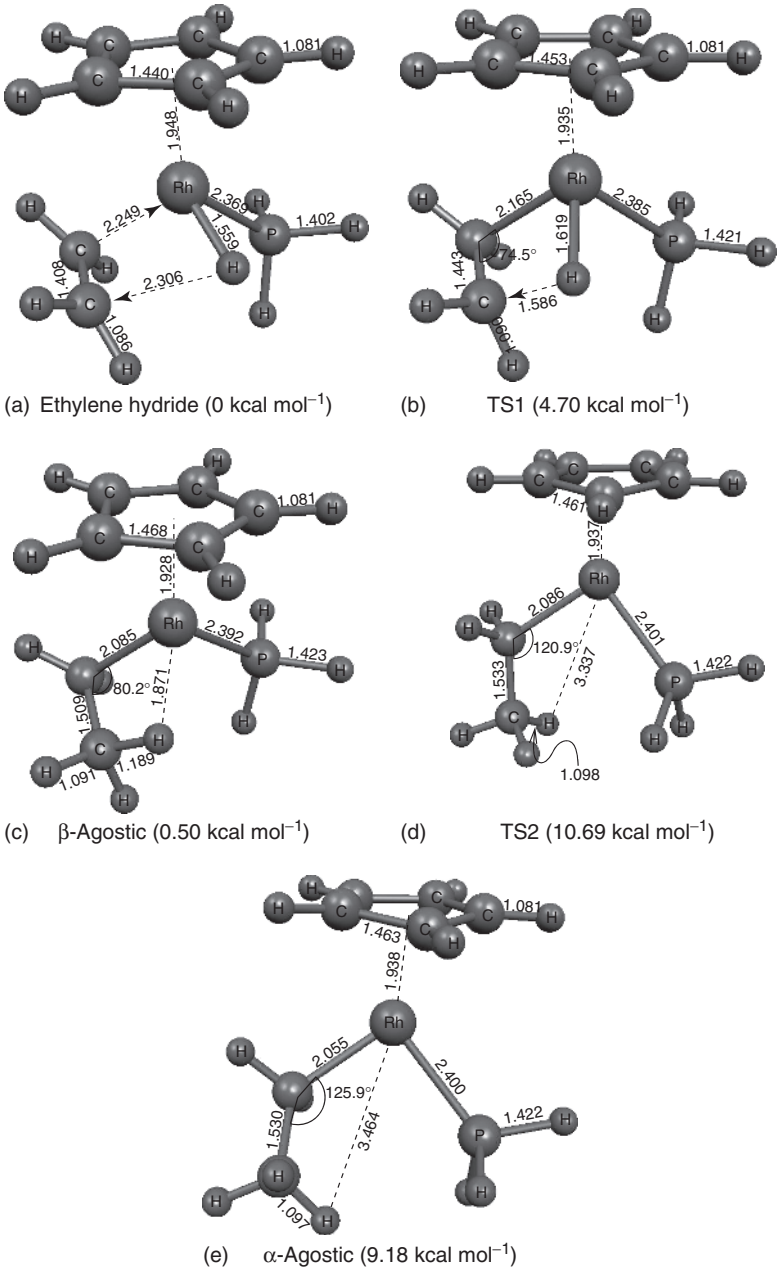

(a) Ethylene hydride (0 kcal mol^{-1}) (b) TS1 (4.70 kcal mol^{-1})

(c) β-Agostic (0.50 kcal mol^{-1}) (d) TS2 (10.69 kcal mol^{-1})

(e) α-Agostic (9.18 kcal mol^{-1})

Figure 1.3 (a–e) Stationary points for the migratory insertion process. B3LYP/SDD geometries and energies of $[CpRh(PH_3)(C_2H_4)]^+$.

the overall insertion process is composed of two distinct steps, which are defined by two characteristic angles [41]:

1) The migration of the hydrogen atom from the TM to the ethylene to form the β-agostic structure (c) is described by the angle $\alpha(C_b-M-H)$; C_b is the carbon atom to which the migrating H will be attached.
2) The opening of the "chain" formed by the TM and the ethylene/ethyl moiety during the transformation of the β-agostic to the α-agostic structure (e) is described by the angle $\beta(M-C_a-C_b)$.

The four atoms involved here are thus considered key to describing the reaction.

A comparison of the energies of the stationary points for Cp-donor-type complexes of the late TMs Co and Rh is presented in Figure 1.4. Depending on the TM under consideration, either the ethylene hydride (Rh) or the β-agostic isomers (Co) represent the global minima, while the α-agostic species and their interconnecting transition states TS2 are rather high in energy. It is seen that the insertion barriers TS1 are negligible for the Co complexes, while the barriers to β-elimination given by $\Delta E = E_{TS1} - E_{\beta\text{-agostic}}$ are more than twice as high for the Co complexes than for any of their Rh analogs. Cobalt polymerization catalysts are therefore expected to exhibit less β-elimination and thus generate polymer of higher molecular weight and with less branching. Indeed, the complex $[Cp^*Co(P(OMe)_3)(Pr)]^+$ is an active polymerization catalyst [42]. If the phosphine ligands for the Co complexes are ordered according to barrier height ΔE, the following series is obtained:

$$PMe_3 \approx P(OMe)_3 < PH_3 < PF_3$$

Transition state theory thus predicts that the importance of β-elimination should diminish in the same order and identifies PF_3 as the ligand conferring

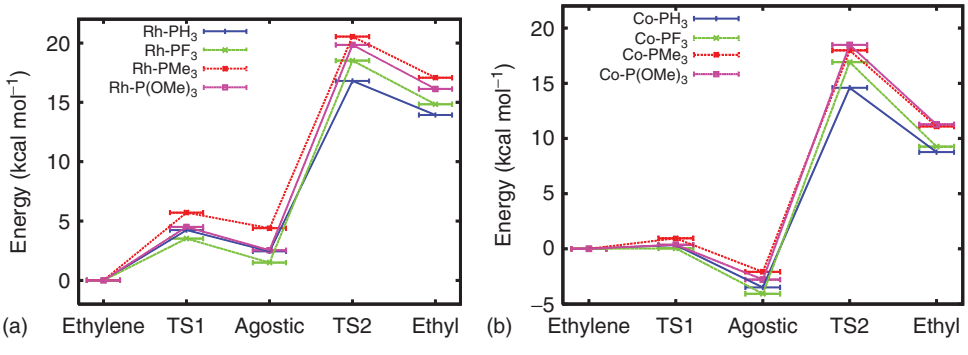

Figure 1.4 (a,b) Relative electronic energies (without zero-point energy) for the $[CpM(L)(H)C_2H_4]^+$ complexes. The energy of the ethylene structure is always set to 0. The other energies are defined in relation to the ethylene structure.

the greatest stability to the agostic intermediate. The relative energy barriers for the β-elimination step of the Co complexes increase approximately in the same order as the electron acceptor strengths of the ligands. For the Rh complexes, the analogous ligand order is found to be $PMe_3 < PH_3 < PF_3 < P(OMe)_3$.

The correlation with the ligand donor/acceptor strength is less clear in this case, but it is noteworthy nevertheless that the lowest ΔE values for both metals occur for the strong donor PMe_3 [43].

In addition to migratory insertion/BHE, the aforementioned complexes are subject to further dynamical processes. Four nuclear (C/H) scrambling processes have been examined theoretically; their computed activation energies agree very well with data from NMR studies [44].

1.3 Quantum Dynamical Calculations

1.3.1 Reaction Path Energy Profiles

Quantum dynamics is the propagation of a wave packet on a (in general) multidimensional PES according to the time-dependent Schrödinger equation. While Figure 1.4 provides an overview of the five stationary points of the PES for the insertion/elimination process, more detailed information about the energy variation in the course of the reaction is required. For a one-dimensional analysis confined to the reaction coordinate only, this can be obtained from either *ab initio* or DFT calculations by the IRC approach [45–48]. Zero-point effects may then be accounted for by a linear interpolation scheme. The reaction path energy curves for insertion/elimination in the $[CpM(L)(H)(C_2H_4)]^+$ complexes (M = Co, Rh; L = PMe_3, $P(OMe)_3$, PH_3, PF_3) are shown in Figure 1.5.

Inspection of the IRC reaction paths reveals that not all the five stationary points mentioned previously can be identified on all curves. Disregarding the complexes with the electron-rich PMe_3 ligand, we observe that for the Rh complexes TS1 corresponds to a narrow barrier, while for the Co complexes this barrier completely disappears after the zero-point energy (ZPE) correction is applied. This indicates that, from an energetic point of view, the first part of the migratory insertion (from the ethylene to the β-agostic conformation) is very fast for these complexes and should be easily observed at room temperature. Interestingly, the IRC curve for the Rh–PMe_3 complex is characterized by the absence of an agostic minimum, which would indicate that this compound might be the least effective as a polymerization catalyst. In contrast, the analogous Co complex is the only one for which a small TS1 insertion barrier is observed. For the second transition state TS2, we find a much broader and higher barrier for all complexes of both TMs.

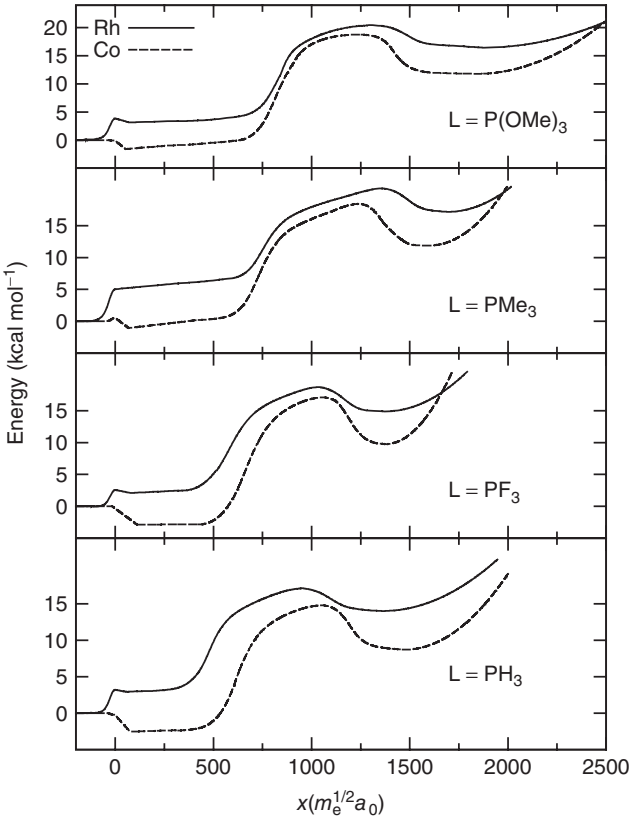

Figure 1.5 Zero-point energy-corrected potential energy curves along the reaction path in mass-weighted intrinsic coordinates for the complexes $[CpM(L)(H)C_2H_4]^+$.

1.3.2
Wave Packet Propagation for Late-Transition-Metal Complexes

If the wave packet maximum is traced along the reaction coordinate as a function of time, system-specific oscillation periods T may be determined. Figure 1.6 portrays the oscillation of the wave packet representing the $[CpRh(PH_3)(H)(C_2H_4)]^+$ complex within the agostic minimum for a start at TS1.

It is seen that, after 12 fs, the wave packet splits into two parts, moving to the left and to the right, respectively. The part on the left-hand side represents the molecules that isomerize to the ethylene complex. These parts are absorbed by a complex absorbing potential (CAP) that simulates decay of the complex, and they disappear for $t > 80$ fs. The part that moves along the right-hand side of the barrier runs into the local minimum of the β-agostic structure. It evolves further to the TS2 barrier, where it is reflected at 144 fs. Subsequently, the wave packet returns to the TS1 barrier, where a part of it overcomes the barrier and is thus

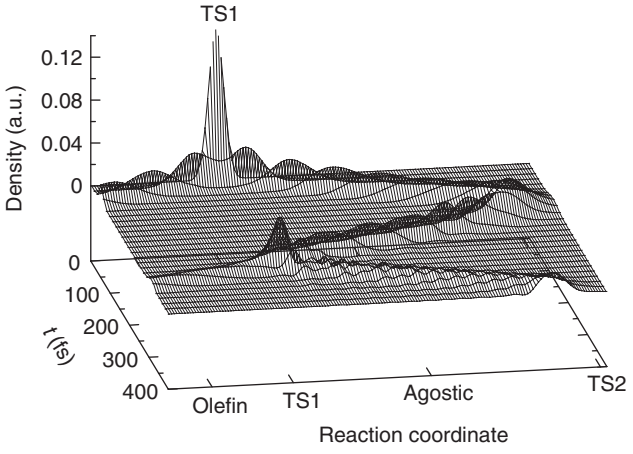

Figure 1.6 Oscillation of the time-dependent wave function within the β-agostic minimum for an initial wave packet located at TS1.

absorbed by the CAP. The rest of the packet continues to oscillate in the β-agostic minimum. During each oscillation period, a part of the wave packet is absorbed by the CAP.

Quantum dynamical simulations involving 2D and 3D PESs have also been performed. In the former case, the reaction is described by the reaction coordinates γ and θ, which are closely related to the angles α and β describing the two steps of the insertion process that have been defined in the previous section, while the latter additionally includes the metal–hydrogen bond length R_H, which was fixed to its value for the β-agostic minimum for the 2D PES. Figure 1.7 shows the 2D dynamics of a wave packet evolving from a saddle point on the $V(\gamma,\theta)$ surface which was visually identified to correspond to TS1 on the 3D PES after its center had been placed at this "quasi-TS1" at $t = 0$.

The reaction path is given in this figure by the black line that connects the stationary points (black dots). When the wave packet propagates, it splits up in two parts. One part propagates toward the ethylene minimum located near the top of the panels and is absorbed by the CAP. The other part of the wave packet moves into the agostic minimum where it oscillates (see panels for 32 fs and later). The potential close to the agostic minimum can be compared with a 2D harmonic potential. Each time the packet reaches TS1, a part of the packet evolves toward the ethylene minimum and will be absorbed by the CAP. As time increases, more and more molecules undergo the elimination process, and the wave packet gradually decays.

Figure 1.8 shows the time-dependent wave function resulting from the 3D calculation as a contour plot. In the first 5 fs, the wave packet is moving in the R_H direction because of the small reduced mass μ_H determining this motion. After 10 fs, the wave packet concentrates in the β-agostic minimum. Its subsequent oscillation and broadening in the β-agostic minimum is followed by a splitting

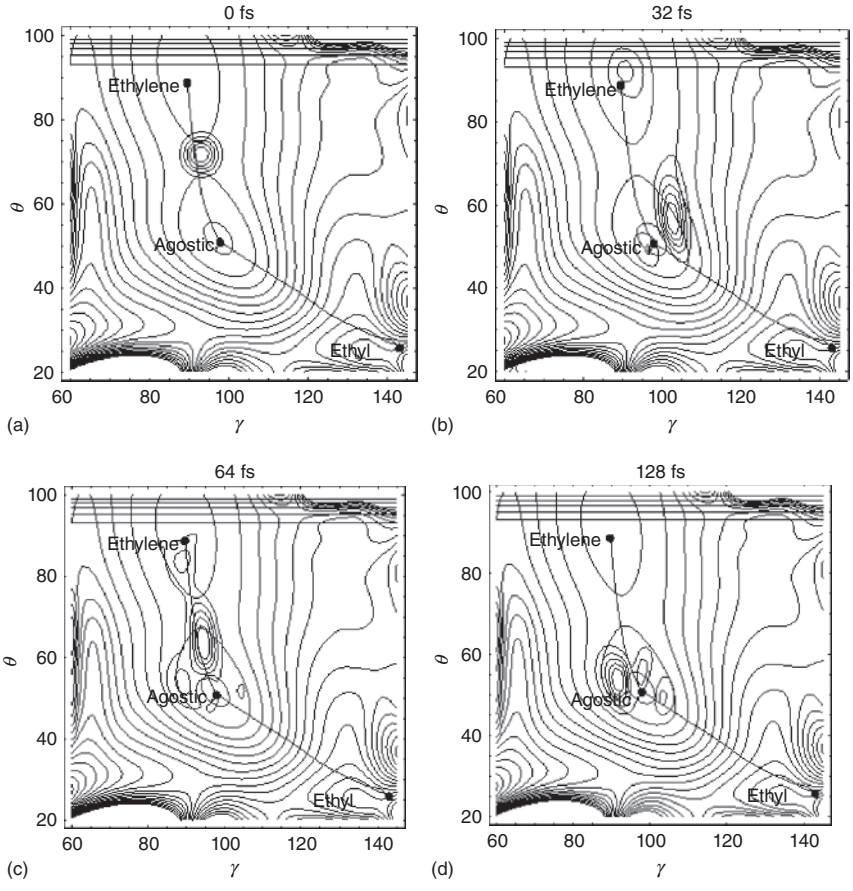

Figure 1.7 (a–d) Snapshots of the 2D time evolution of a wave packet started at quasi-TS1 on the agostic PES. Angles are in degrees.

into two parts. One part oscillates in the β-agostic minimum, while the other part moves toward the ethylene minimum, where it is absorbed by the CAP (20 fs and later). This process goes on periodically, and qualitatively in the same way as in the 1D and 2D calculations [49].

1.3.3
Norm Decay and Lifetimes

The overall progress of a wave packet propagation can be monitored by plotting the squared norm $N^2(t)$ of the wave packet as a function of time. Figure 1.9 presents the time evolutions of these survival probabilities of respective wave packets starting at TS1/ES (ethylene structure) and TS2 for all Co and Rh TM

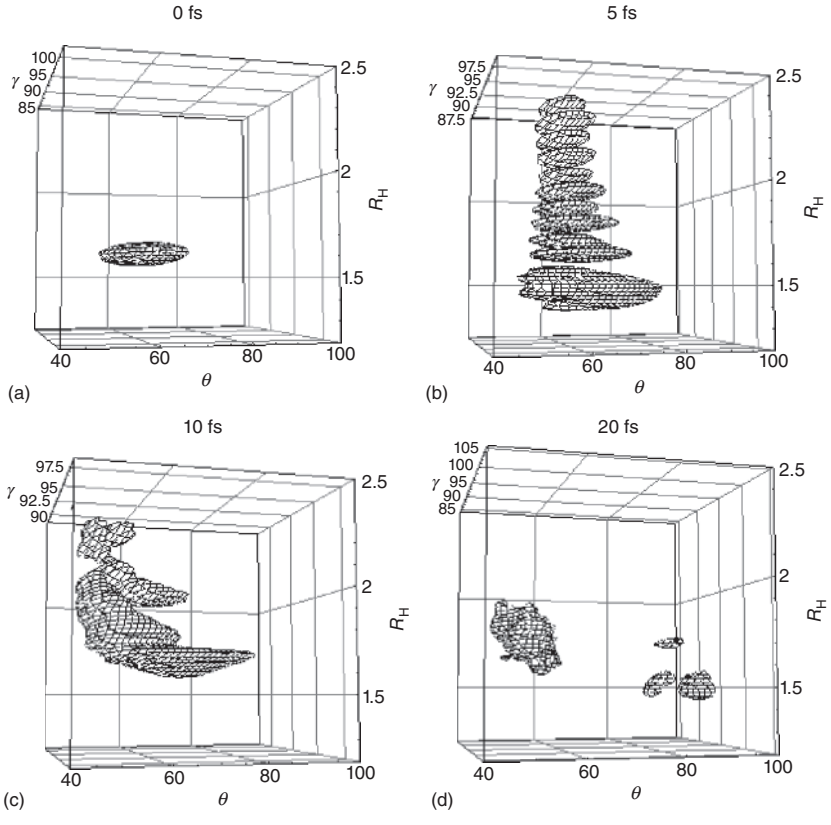

Figure 1.8 (a–d) Snapshots of the 3D time evolution of a wave packet started at TS1. Angles are given in degrees, R_H in angstrom. The contours correspond to a probability of $|\Psi(t)|^2 = 10^{-4}$.

complexes investigated.[2)] An exponential fit of $N^2(t)$ is also plotted. The squared norm decreases in a stepwise manner over time. The steps are nearly equidistant, with the distance corresponding to an oscillation period T of the wave packet moving in the respective minimum region (agostic for the initial wave packet located at TS1/ES, ethyl for the initial wave packet located at TS2). The steep sections of $N^2(t)$ correspond to the absorption of that part of the wave packet that has penetrated the region of the TS1 barrier and moved into the CAP region. Consequently, T can be obtained by inspecting the time evolution of $N^2(t)$. For instance, for a wave packet originating at TS2 for the ethyl minimum of the $Rh-PF_3$ complex, it is thus estimated to be 430 fs, and this value is close to that found by tracing the wave packet (454 fs). For each ligand L, the T_L for the Rh complex are longer than for the corresponding Co complex. This is because the

2) For all but one of the Co complexes, the TS1 barrier disappears after zero point correction. Wave packets are started from the ES in these cases.

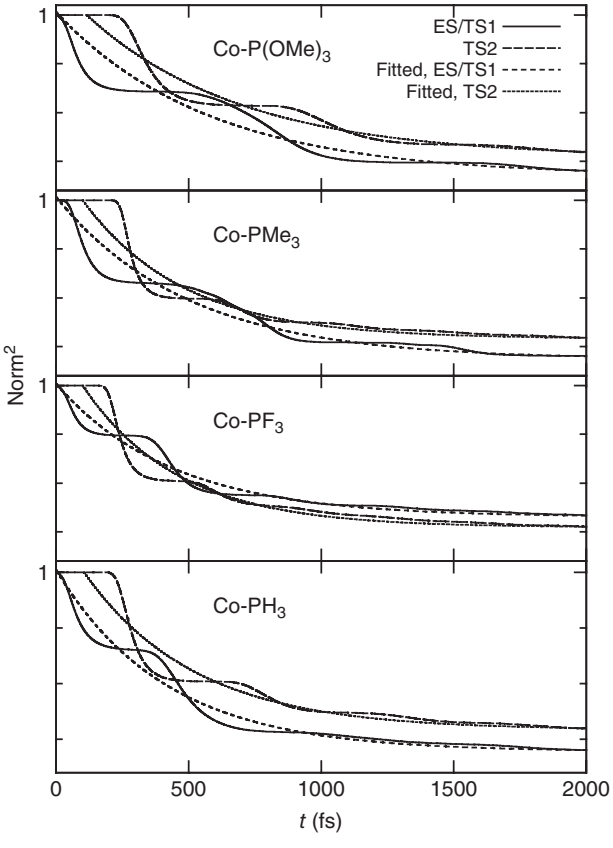

Figure 1.9 Time evolution of the squared norm (survival probabilities) for one-dimensional wave packets started at TS1 or TS2 for the $[CpCo(L)H(C_2H_4)]^+$ complexes. The fitted norm is based on $y = (1-c)e^{-t/\tau} + c$.

higher ΔE values for the Co complex will result in faster propagation in the agostic potential well (due to its anharmonicity) and hence a shorter oscillation period. Since the ΔE values do not drastically differ among the Co complexes, we find that their T_L values increase in line with the ligand mass. Except for $L = PMe_3$, this correlation also holds for the Rh complexes. The short T for the trimethylphosphine ligand is due to its lack of an agostic minimum; instead of a genuine oscillation one therefore observes a complete decay of the norm after two absorption steps for this system. It is seen that the decay of $N^2(t)$ is almost complete after the first few oscillation periods. This process can be ascribed to the decay of the respective complex due to H-elimination following broadband excitation to TS1/ES or TS2. The lifetime τ of the system can be determined by fitting an exponential decay function to $N^2(t)$ and can be considered an indicator for the stability of the catalyst's β-agostic state against β-elimination. When comparing the τ_L for the same TM, it is found that they increase in parallel with

T_L: that is, a ligand with a longer oscillation time will also increase the lifetime of a particular complex. However, for identical ligands L, the lifetimes for the Co complexes are longer than for the Rh complexes. This is a consequence of the considerably lower energies (by over 2 kcal mol^{-1}) of the wave packet starting points at ES/TS1 for M = Co, resulting in a slower propagation in the region of the ES and the CAP. Our quantum dynamical results demonstrate that the broadband excitation lifetimes and hence the stability against β-elimination are influenced by the dynamics in both the agostic region and the ethylene region. For any particular ligand, cobalt catalysts are expected to generate a polymer that is characterized by higher molecular weight and less branching. Comparing the four ligands, we expect catalysts with L = $P(OMe)_3$ to lead to a polymer with the highest molecular weight. Indeed, the catalyst $[Cp^*Co(P(OMe)_3)(Pr)]^+$ is used in the living polymerization of ethylene [50]. Data comparing the molecular mass and degree of branching for a polymer synthesized by a variety of late TM catalysts could corroborate our model once they become available.

1.3.4
Quantum Dynamics of Ethylene Insertion in Chromium Complexes

To contrast our findings for late TMs with data from a metal situated earlier in the d-block, we return to the Cp-donor-based chromium–alkyl complexes already addressed in Section 1.2.

The reaction path energy curve for insertion in the $[CpCr(PH_3)CH_3]^+$ complex in Figure 1.10 consists of five sections. The middle three parts correspond to IRC calculations starting from the transition states [II* → I], [I → IIγ], and [IIγ → IIα],

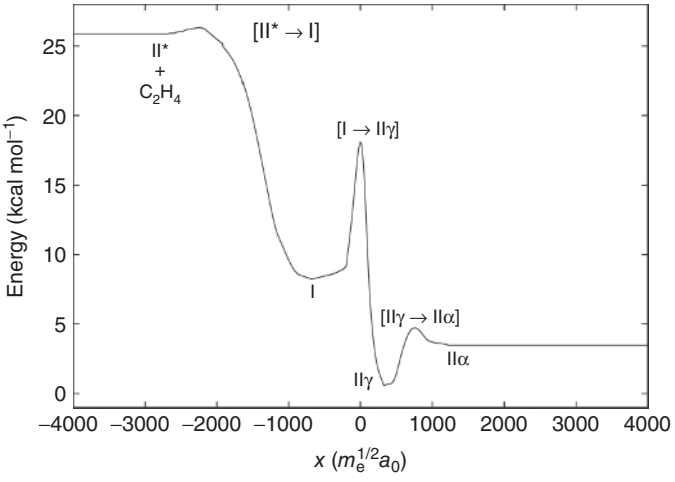

Figure 1.10 Zero-point energy-corrected potential energy curve along the reaction path in mass-weighted intrinsic coordinate for the complex $[CpCr(PH_3)CH_3]^+$. II* designates the structure of the methyl complex before the coordination of ethylene.

respectively, where II* is formed from I by dissociation of the coordinated ethylene. The two outermost parts serve to provide an extension of the grid range to the left and right, beyond structures IIα and II*, in order to enable the study of reactions by adding a CAP. As already mentioned, the actual reaction path is branched because the IIγ isomer may convert into either the IIα or the IIβ isomer; the IIα isomer has been selected here for illustrative purposes.

The IRC curves provide a direct and convenient way to probe the change of the energy and the structure of the complex along the reaction path. Consequently, the reaction sequence can be deduced from an analysis of the IRC curves. It is seen that the dissociated ES II* is about 18 kcal mol^{-1} above the ethylene–alkyl complex I, and the transition state [II* → I] for this dissociation still about 7 kcal mol^{-1} higher than the transition state [I → IIγ]. We therefore do not expect the dissociation of monomers from the complex to occur on the same time scale as the chain growth and subsequent isomerization of the insertion product. Indeed, the wave packet did not advance to the region of II* during our simulations. In comparison with the profiles for late TMs in Figure 1.5, the [I → IIγ] barrier (corresponding to TS1) is relatively high (10.1 kcal mol^{-1}), because here insertion into a metal–alkyl bond is considered. Furthermore, the agostic isomers are now considerably more stable than the ES, which is reflected in the diminished role of β-elimination in these systems. The energy differences of the agostic isomers and the barriers separating them (corresponding to TS2) are relatively small; their rapid interconversion is to be expected.

Inspection of Figure 1.11a displaying the time-dependent wave function with starting point [I → IIγ] confirms the above scenario. After starting its propagation, the wave packet separates into two parts in a rather short time. One part

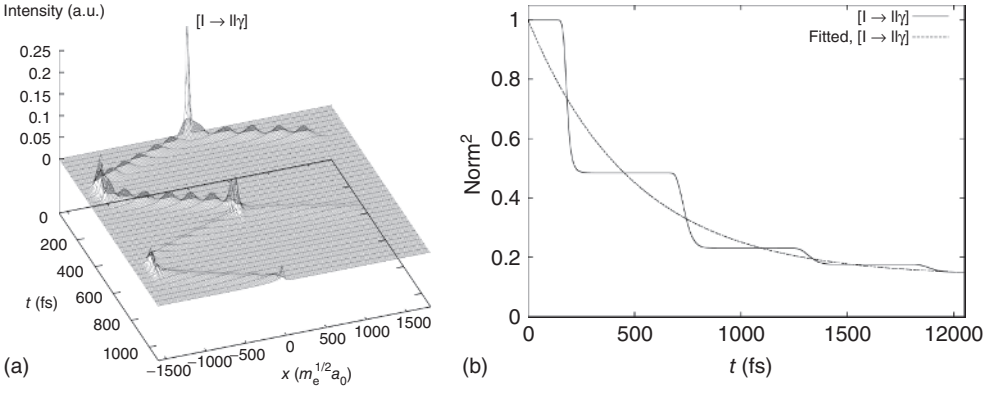

Figure 1.11 (a) Oscillation of the time-dependent wave function along the reaction coordinate for $[CpCr(PH_3)CH_3]^+$. The transition state $[I \rightarrow II\gamma]^{\ddagger}(^4A)$ was selected as the starting point for the propagation. (b) Time evolution of the squared norm for a one-dimensional wave packet starting at $[I \rightarrow II\gamma](^4A)$ for $[CpCr(PH_3)CH_3]^+$. The fitted squared norm is based on $y = (1 - c)e^{-t/\tau} + c$.

propagates to the right of the barrier formed by [I → IIγ], moving into the potential energy well of the γ-agostic minimum, and further over the [IIγ → IIα] barrier to the region of the α-agostic minimum. It will be absorbed by the CAP after it has passed through this minimum (i.e., for $x > 1226\ m_e^{1/2} a_0$). Therefore, this part of the wave packet describes the migratory insertion of the complex.

The other part of the wave packet propagates toward the left-hand side of the barrier formed by [I → IIγ], where it starts to oscillate. This part of the packet represents the molecules isomerizing to the ethylene complex I.

During each oscillation period, this wave packet evolves from the [I → IIγ] barrier toward the region of [II* → I], where it is reflected. It then proceeds back to the [I → IIγ] barrier, whereupon a part of the packet penetrates the barrier and subsequently evolves toward the α-agostic minimum and is absorbed by the CAP. The rest of the packet continues to oscillate in the ethylene minimum. Each time the packet completes an oscillation and reaches the [I → IIγ] barrier, a part of the packet overcomes the barrier and is absorbed by the CAP. As time increases, a larger and larger part of the wave packet is absorbed. This reflects the increasing probability for the complex to undergo migratory insertion. It is noteworthy that the region below $x = -2000$ is never reached by the wave packet during the simulation, which confirms the longer time scale and lower significance of monomer dissociation for our model catalyst.

The overall progress of a wave packet propagation can be monitored by plotting the square of the norm $N^2(t)$ of the wave function as a function of time. Figure 1.11b presents the time evolution of the squared norm starting at [I → IIγ] for $[CpCr(PH_3)CH_3]^+$. An exponential fit of the squared norm is also plotted, from which the lifetime τ of the system can be determined. In this case, τ measures the stability of the catalyst against migratory insertion, while for the late TM complexes described above it refers to stability against β-elimination, due to the different positioning of the CAP. Hence, the dynamics data derived for the two situations, for example, from the norm decays given in Figures 1.9 and 1.11b, are not directly comparable.

As shown in Figure 1.11b, the squared norm of the wave packet at the beginning of the propagation is set to 1. It then decreases in a stepwise fashion over time. The steps are nearly equidistant, with the distance corresponding to an oscillation period of the wave packet moving in the ethylene minimum region. The sections of steep decay of $N^2(t)$ correspond to the absorption of that part of the wave packet that has penetrated the region of the [I → IIγ] barrier and moved into the CAP region. By tracing the position of the wave packet maximum during the propagation, we obtained a value of $T = 590$ fs for the aforementioned complex. From Figure 1.11b, it is seen that the squared norm of a wave packet has decayed to about 20% after the first few oscillation periods. This corresponds to the migratory insertion reaction of the respective complex. The lifetime obtained for $[CpCr(PH_3)CH_3]^+$ is $\tau = 500$ fs.

1.4 Summary and Outlook

In this chapter, we have described a quantal approach to investigate the dynamics of elementary catalytic reaction steps, especially BHE from an agostic TM complex. Several reduced-dimensionality (1D–3D) treatments could be set up, and many new spectroscopic data and time constants (vibrational periods and lifetimes) were obtained, which shed new light on the species treated and on the process in general. Further improvement of the dynamical approach would consist in including additional degrees of freedom; however, the latter would require a more approximate treatment, such as a locally harmonic approximation, to save computational effort in generating the DFT PES. As a further step in the overall line of investigation, these studies are to be extended to the computation of thermal rate constants. (Remember that the present study focused on a highly nonequilibrium process, corresponding to a Franck–Condon excitation to the transition states of the system.) This is possible, for example, by utilizing the above techniques and results within the flux–flux correlation function formalism of Miller, Manthe *et al.* [51, 52]. Of particular interest in this context are rate calculations for hydrogen transfer reactions, because of the importance of tunneling and barrier-recrossing effects in these systems. A preliminary study of the isotope effect on migratory insertion confirmed the expected deviation from Arrhenius-type dynamics at low temperatures. It is hoped that these studies will provide more insight into the electronic factors governing, for example, the outcome of olefin polymerization, and thus help in its control. More generally, we point out the relevance of our reduced-dimensionality treatment to processes other than those investigated here. The above-mentioned four atoms explicitly retained in our description are the atoms between which bonds are broken and formed in the course of the reaction. The present analysis establishes that it is mostly their structural parameters that change significantly, whereas the others remain nearly constant. If this holds true also for other systems, it might open a route to extend this approach to a large variety of different reactive processes, catalytic and others.

Acknowledgments

This work was financially supported by the German Research Council (DFG) through SFB623 "Molekulare Katalysatoren: Struktur und Funktionsdesign." The authors are indebted to Markus Enders for helpful discussions.

References

1. Koga, K. and Morokuma, K. (1991) *Chem. Rev.*, **91**, 823.
2. Musaev, D.G. and Morokuma, K. (1996) *Adv. Chem. Phys.*, **95**, 61.
3. Ziegler, T. (1991) *Chem. Rev.*, **91**, 651.
4. Salahub, D.R., Castro, M., Fournier, R., Calaminici, P., Godbout, N., Goursot, A., Jamorski, C., Kobayashi, H., Martinez,

A., Papai, I., Proynow, E., Russo, N., Sirois, S., Ushio, J., and Vela, A. (1995) in *Theoretical and Computational Approaches to Interface Phenomena* (eds H. Sellers and J. Olab), Plenum Press, New York, p. 817.
5. Siegbahn, P.E.M. (1996) *Adv. Chem. Phys.*, **93**, 333.
6. Dedieu, A. (ed.) (1992) *Transition Metal Hydrides*, VCH Publishers, New York.
7. van Leeuwen, P.W., van Lenthe, J.H., and Morokuma, K. (eds) (1994) *Theoretical Aspects of Homogeneous Catalysts. Applications of ab initio Molecular Orbital Theory*, Kluwer Academic Publishers, Dordrecht.
8. Yoshida, S., Sakaki, S., and Kobayashi, H. (1992) *Electronic Processes in Catalysis*, VCH Publishers, New York.
9. Brookhart, M., Green, M.L.H., and Wong, L.-L. (1988) *Prog. Inorg. Chem.*, **36**, 1.
10. Brookhart, M., Lincoln, D.M., Volpe, A.F., and Schmidt, G.F. (1989) *Organometallics*, **8**, 1212.
11. Brookhart, M., Hauptman, E., and Lincoln, D.M. (1992) *J. Am. Chem. Soc.*, **114**, 10394.
12. Ittel, S.D., Johnson, L.K., and Brookhart, M. (2000) *Chem. Rev.*, **100**, 1169.
13. Ziegler, K., Holzkamp, E., Breil, H., and Martin, H. (1955) *Angew. Chem.*, **67**, 541.
14. Ziegler, K. (1964) *Angew. Chem.*, **76**, 545.
15. Natta, G. and Corradini, P. (1955) *Atti. Accad. Naz. Lincei Mem. CI. Sci. Fis. Mat. Nat. Sez. II*, **5**, 73.
16. Natta, G. (1956) *Angew. Chem.*, **68**, 393.
17. Natta, G. (1964) *Angew. Chem.*, **76**, 553.
18. Seymour, R.B. and Cheng, T. (eds) (1986) *History of Polyolefins*, Reidel, Dordrecht.
19. Eisch, J.J. (1983) *J. Chem. Educ.*, **60**, 1009.
20. Boor, J. (1979) *Ziegler-Natta Catalysts and Polymerisations*, Academic Press, New York.
21. Sinn, H. and Kaminsky, W. (1980) *Adv. Organomet. Chem.*, **18**, 99.
22. Pino, P. and Mülhaupt, R. (1980) *Angew. Chem., Int. Ed. Engl.*, **19**, 857.
23. Hogan, J.P. and Banks, R.L. (1955) (Phillips Petroleum Co.) Belg Patent 530,617; U.S. Patent 2825,721, 1958.
24. Hogan, J.P. (1970) *J. Polym. Sci. A*, **8**, 2637.
25. Groppo, E., Lamberti, C., Bordiga, S., Spoto, G., and Zecchina, A. (2005) *Chem. Rev.*, **105**, 115.
26. Döhring, A., Jensen, V.R., Jolly, P.W., Thiel, W., and Weber, J.C. (2001) *Organometallics*, **20**, 2234.
27. Johnson, L.K., Killian, C.M., and Brookhart, M. (1995) *J. Am. Chem. Soc.*, **117**, 6414.
28. Ziegler, T. and Autschbach, J. (2005) *Chem. Rev.*, **105**, 2695.
29. Schork, R. and Köppel, H. (2001) *J. Chem. Phys.*, **115**, 7907.
30. Mahapatra, S., Köppel, H., and Cederbaum, L.S. (2001) *J. Phys. Chem.*, **105**, 2321.
31. Somers, M.F., Kingma, S.M., Pijper, E., Kroes, G.J., and Lemoine, D. (2002) *Chem. Phys. Lett.*, **360**, 390.
32. Kulander, K.C. (1991) *Time-dependent Methods for Quantum Dynamics*, North-Holland Publishing Company.
33. Zhang, J.Z. (1999) *Theory and Application of Quantum Molecular Dynamics*, World Scientific, River Edge, NJ.
34. Senn, H.M., Blöchel, P., and Togni, A. (2000) *J. Am. Chem. Soc.*, **122**, 4098.
35. Meier, R.J., van Doremaele, G.H., Ialori, S., and Buda, F. (1994) *J. Am. Chem. Soc.*, **116**, 7274.
36. Zewail, A.H. (1999) Atomic-Scale Dynamics of the Chemical Bond Using Ultrafast Lasers. Nobel Lecture.
37. Zewail, A.H. (1994) *Femtochemistry*, vol. 1 and 2, World Scientific, Singapore.
38. Manz, J. and Wöste, L. (1995) *Femtosecond Chemistry*, Verlag Chemie, Weinheim.
39. Xu, R., Klatt, G., Enders, M., and Köppel, H. (2012) *J. Phys. Chem. A*, **116**, 1077.
40. Mark, S., Kurek, A., Mülhaupt, R., Xu, R., Klatt, G., Köppel, H., and Enders, M. (2010) *Angew. Chem. Int. Ed.*, **49**, 8751.
41. Bittner, M. and Köppel, H. (2004) *J. Phys. Chem. A*, **108**, 11116.
42. Daugulis, O., Brookhart, M., and White, P.S. (2003) *Organometallics*, **22**, 4699.

43. Xu, R., Bittner, M., Klatt, G., and Köppel, H. (2008) *J. Phys. Chem. A*, **112**, 13139.
44. Xu, R., Klatt, G., Wadepohl, H., and Köppel, H. (2010) *Inorg. Chem.*, **49**, 3289.
45. Fukui, K., Sato, S., and Fujimoto, H. (1975) *J. Am. Chem. Soc.*, **97**, 1.
46. Fukui, K. (1981) *Adv. Chem. Phys.*, **14**, 363.
47. Gonzalez, C. and Schlegel, H.B. (1989) *J. Phys. Chem.*, **90**, 2154.
48. Gonzalez, C. and Schlegel, H.B. (1990) *J. Phys. Chem.*, **94**, 5523.
49. Bittner, M., Köppel, H., and Gatti, F. (2007) *J. Phys. Chem. A*, **111**, 2407.
50. Tanner, M.J., Brookhart, M., and DeSimone, J.M. (1997) *J. Am. Chem. Soc.*, **119**, 7617.
51. Miller, W., Schwartz, S., and Tromp, J. (1983) *J. Chem. Phys.*, **79**, 4889.
52. Manthe, U. (2002) *J. Theor. Comput. Chem.*, **1**, 153.